REPORT

Stable perovskite solar cells with efficiency exceeding 24.8% and 0.3-V voltage loss

Mingyu Jeong[1]*, In Woo Choi[2,3]*, Eun Min Go[4]*, Yongjoon Cho[1], Minjin Kim[2], Byongkyu Lee[1], Seonghun Jeong[1], Yimhyun Jo[2], Hye Won Choi[2], Jiyun Lee[4], Jin-Hyuk Bae[3], Sang Kyu Kwak[4]†, Dong Suk Kim[2]†, Changduk Yang[1]†

Further improvement and stabilization of perovskite solar cell (PSC) performance are essential to achieve the commercial viability of next-generation photovoltaics. Considering the benefits of fluorination to conjugated materials for energy levels, hydrophobicity, and noncovalent interactions, two fluorinated isomeric analogs of the well-known hole-transporting material (HTM) Spiro-OMeTAD are developed and used as HTMs in PSCs. The structure–property relationship induced by constitutional isomerism is investigated through experimental, atomistic, and theoretical analyses, and the fabricated PSCs feature high efficiency up to 24.82% (certified at 24.64% with 0.3-volt voltage loss), along with long-term stability in wet conditions without encapsulation (87% efficiency retention after 500 hours). We also achieve an efficiency of 22.31% in the large-area cell.

To achieve better and cheaper alternative energy, perovskite solar cells (PSCs) have been the front runner among emerging next-generation solar cells. Power conversion efficiency (PCE) exceeding 25% (1) has been achieved in laboratory-scale PSCs by improving the perovskite material formulations (2–5), the device fabrication routines (6–9), and the high-quality film-formation methodologies (10–12) on the basis of a comprehensive understanding of the charge dynamics at the interfacial layers. Most high-performance PSCs have a sandwich structure composed of a perovskite absorber between a metal oxide–based electron-transporting material (ETM) and an organic hole-transporting material (HTM) (3, 7, 13, 14). Because high-quality perovskite and ETMs can be obtained from various processing methodologies, HTMs are considered to be fundamentally important in further improving PSC performance. Despite efforts to develop better HTMs to replace Spiro-OMeTAD [2,2′,7,7′-tetrakis(N,N-di-p-methoxyphenylamine)-9,9′-spirobifluorene] (15–17), this compound, which was developed by Grätzel et al. for solid-state dye-sensitized solar cells more than two decades ago (18), is still recognized as the most

efficient HTM in PSCs owing to its amorphous nature, high compatibility with dopants, and energy levels matching those of perovskite. However, it must be chemically doped with hygroscopic dopants to attain efficient hole extraction and sufficient conductivity. Such doping negatively influences the stability of ambient PSCs, thus presenting a major obstacle to truly commercializing PSCs despite PCE being sufficient for practical applications (19–21). Therefore, the PSC community is actively investigating candidate HTMs to replace Spiro-OMeTAD and ultimately achieve stable PSCs simultaneously exhibiting the same or improved performance. Notably, the latest research on cesium cation (Cs⁺)– (22, 23), carbon electrode– (24–26), and dopant-free–based PSCs (27, 28) can bring the benefits in improving the device stability but lower PCE levels when compared with that of the Spiro-OMeTAD–based PSC.

Considering the multiple possible aspects of fluorination of the conjugated materials (e.g., lowering energy levels and enhancing molecular packing and hydrophobicity through the induced dipole along the C–F bond), we developed two fluorinated isomeric analogs (Spiro-mF and Spiro-oF) of Spiro-OMeTAD as HTMs for PSC fabrication and compared their device performance with that of the optimized Spiro-OMeTAD–based PSC. Not only do we report a PCE of 24.82% (certified PCE of 24.64% with 0.3-V loss) achieved from the device fabricated with Spiro-mF, but we also show the long-term stability of fluorinated HTM-based devices without encapsulation on exposure to high relative humidity (RH) (87% PCE retention after 500 hours). Furthermore, the Spiro-mF–based PSC, with an area of 1 cm², represents an efficiency of 22.31%.

Figure 1A presents the chemical structures of the parent Spiro-OMeTAD and its fluorinated analogs (Spiro-mF and Spiro-oF). The two fluorinated isomeric HTMs were synthesized through two Buchwald-Hartwig C–N cross-coupling reactions; detailed synthesis and molecular characterization are described in figs. S1 to S7 and materials and methods. Differential scanning calorimetry analysis revealed that the synthesized HTMs exist in both amorphous and crystalline states, as evidenced by the observation of glass-transition and melting temperatures (fig. S8). The ultraviolet-visible absorption (UV-Vis) spectra in Fig. 1B show that, in addition to the absorption band from 300 to 450 nm, the three HTMs feature a slight redshift as the solution transitions to the solid state, which is commonly observed in many organic semiconductors (29–31). Relative to the Spiro-OMeTAD, both new fluorinated isomeric HTMs, especially Spiro-oF, display obvious blue-shifted absorption maxima and onsets, thus leading to the net widening of their optical bandgaps (E_g^{opt}), which is attributed to the fluorine atoms generating an inductive electron-withdrawing effect on the aromatic rings of the conjugated backbone (32–34). Cyclic voltammetry (CV) was performed on the HTMs to determine the highest occupied molecular orbital (HOMO) energy levels (fig. S9); the lowest unoccupied molecular orbital (LUMO) energy levels were derived from the HOMOs and E_g^{opt}. The CV and E_g^{opt}-derived HOMO and LUMO energies are –4.97 and –2.03, –5.19 and –2.23, and –5.06 and –2.04 eV for Spiro-OMeTAD, Spiro-mF, and Spiro-oF, respectively, thus demonstrating that fluorination can simultaneously lower the HOMO and LUMO levels (Fig. 1C and table S1). These results agree well with the trend estimated from density functional theory (DFT) calculations by using the generalized gradient approximation with Perdew-Burke-Ernzerhof functional (figs. S10 and S11). The same trend is observed for the HOMOs of the doped HTMs (fig. S12). Therefore, in addition to reasonably estimating the enhanced oxidation stability of both fluorinated HTMs, more efficient interfacial hole-transport kinetics are observed compared with that of Spiro-OMeTAD. Moreover, the UV-Vis spectra and CV data indicate a strong fluorine positioning effect, the constitutional isomeric effect, on the optical and electrochemical properties. We also observe clear differences in the DFT-calculated structural conformations and electron distributions of Spiro-mF and Spiro-oF (Fig. 1D).

After deciphering their intrinsic properties, we used Spiro-mF and Spiro-oF as HTMs in PSCs fabricated with the conventional n–i–p configuration, specifically fluorine-doped tin-oxide substrate/compact TiO₂/mesoporous TiO₂/perovskite layer/HTM/Au (fig. S13); FAPbI₃

[1]Department of Energy Engineering, School of Energy and Chemical Engineering, Perovtronics Research Center, Low Dimensional Carbon Materials Center, Ulsan National Institute of Science and Technology (UNIST), Ulju-gun, Ulsan 44919, Republic of Korea. [2]Ulsan Advanced Energy Technology R&D Center, Korea Institute of Energy Research, Nam-gu, Ulsan 44776, Republic of Korea. [3]School of Electronics Engineering, Kyungpook National University, Daegu 41566, Republic of Korea. [4]Department of Energy Engineering, School of Energy and Chemical Engineering, Ulsan National Institute of Science and Technology (UNIST), Ulsan 44919, Republic of Korea.
*These authors contributed equally to this work.
†Corresponding author. Email: yang@unist.ac.kr (C.Y.); kimds@kier.re.kr (D.S.K.); skkwak@unist.ac.kr (S.K.K.)

was selected as the perovskite layer because of its narrow bandgap (1.48 eV), thus making it suitable for the absorption of near-infrared light and promoting thermal stability (*35*, *36*). For a comparative study, we also prepared a control device under the same conditions, using Spiro-OMeTAD as the HTM. The HTM chlorobenzene solution containing 4-*tert*-butylpyridine, lithium bis(trifluoromethanesulfonyl)imide, and tris[2-(1*H*-pyrazol-1-yl)-4-*tert*-butylpyridine]-cobalt(III)-tris[bis-(trifluoromethylsulfonyl)imide] as dopant additives was deposited by spin-coating on the FAPbI$_3$ layer. X-ray diffraction (XRD) patterns of the neat FAPbI$_3$ (fig. S14) show strong diffraction peaks at 14.1° and 28.2°, corresponding to the (001) and (002) crystal planes, respectively, and confirming a dense and ordered perovskite crystal structure. Similar results were observed after the films were spin-coated with the doped HTM solutions, indicating that the HTM processing did not damage the perovskite crystal quality. The optimized thicknesses of the FAPbI$_3$ and HTM layers were ~750 and ~270 nm, respectively. Because PSC performance is sensitive to the dopant type and doping conditions, independent device optimization was also undertaken by carefully screening the ratios and amount of dopant additives. Details about the device fabrication and all device data examined herein are included in the supplementary materials.

Figure 2 shows the current density-voltage (*J-V*) curves of the best PSCs for each given HTM under AM 1.5 G simulated solar illumination at 100 mW cm^{-2}; the corresponding photovoltaic parameters are summarized in table S2. A tiny hysteresis was observed in the *J-V* scans between reverse and forward scans in all cases. First, under optimized conditions, the control device fabricated with Spiro-OMeTAD achieved a maximum PCE of 23.44% for an area of 0.0819 cm^2 with a short-circuit current density (*J*$_{SC}$) of 26.04 mA cm^{-2}, an open-circuit voltage (*V*$_{OC}$) of 1.152 V, and a fill factor (FF) of 78.13%; this value is fairly comparable to the previously reported highest PCE of the PSCs in single-junction devices (*37–39*). Compared with the control device fabricated with doped Spiro-OMeTAD, both fluorinated HTM-based PSCs exhibited nearly identical (*J*$_{SC}$) values of 26.34 to 26.35 mA cm^{-2} and slightly superior *V*$_{OC}$ values over 1.16 V, thus reflecting the lower-lying HOMO levels observed in the CV data. The Spiro-*m*F–based device produced a somewhat higher FF (80.90%) than that of the other devices, ultimately resulting in the best PCE of 24.82%. The slightly lower performance in the forward scan is mainly due to the low FF. The small standard deviation of the PCEs among the tested devices points toward excellent reproducibility (Fig. 2D). PSC performance is highly sensitive to environmental conditions. Thus, to provide accuracy and reproducibility of the device
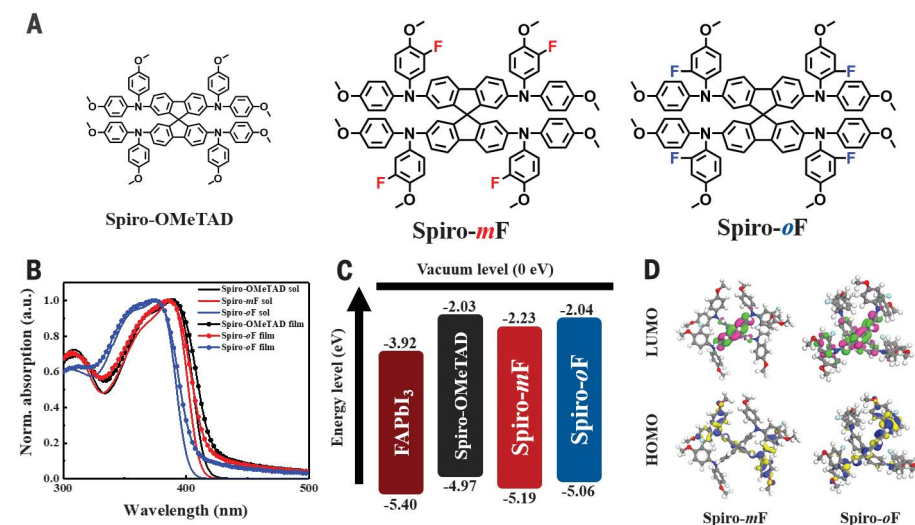
performance metrics reported in Fig. 2D and table S2, we fabricated each device under the same conditions: at 25°C and below 30% RH, with exclusion of strong light and oxygen. One of the best Spiro-*m*F–based devices was sent to an independent solar cell–accredited laboratory (Newport, Irvine, CA, USA) for certification, where a stabilized PCE of 24.64% (with *V*$_{OC}$ = 1.1814 V, *J*$_{SC}$ = 26.1783 mA cm^{-2}, and FF = 79.6%) was confirmed (fig. S16). On the basis of the bandgap of FAPbI$_3$ (1.48 eV), the obtained *V*$_{OC}$ value quantifies the *V*$_{OC}$ loss as 0.3 V, thus being close to the theoretical minimum value based on the radiative limit defined by the Shockley-Queisser theory (*40*, *41*). Because the radiative limit is the near-maximum theoretical PCE of the solar cell, these results suggest that the non-radiative recombination of the device is largely suppressed in the Spiro-*m*F–based PSC, which is directly evidenced by external electroluminescence quantum efficiency (EL-EQE) measurement (fig. S17) (*42*). The reported 0.3-V *V*$_{OC}$ loss is, to the best of our knowledge, the lowest reported value to date for PSCs in any type of device. To demonstrate practical applicability and scalability of the Spiro-*m*F–based device, we also prepared a large-area cell with an area of 1 cm^2, yielding the highest PCE of 22.31% with corresponding *V*$_{OC}$, *J*$_{SC}$, and FF of 1.178 V, 25.51 mA cm^{-2}, and 74.22%, as shown in Fig. 2E. By using space charge–limited current (SCLC) measurements, the hole mobility (μ) of the pristine HTMs is in order of Spiro-OMeTAD (6.5904 × 10^{-3} cm^2 V^{-1} s^{-1}) < Spiro-*o*F (7.2902 × 10^{-3} cm^2 V^{-1} s^{-1}) < Spiro-*m*F (7.4748 × 10^{-3} cm^2 V^{-1} s^{-1}) (fig. S18). The higher μ in Spiro-*m*F can be explained by denser solid-

state packing through noncovalent inter- and intra-interactions induced by F atoms (*43*, *44*), corresponding to the slightly enhanced *J*$_{SC}$ and FF values of the Spiro-*m*F–based PSC. By contrast, in Spiro-*o*F, the outward appended F atoms of the central HTM unit may act as a steric hindrance such that intermolecular interaction is dampened, hence making it more difficult for the charge to hop between molecules (the more bent structure of Spiro-*o*F core relative to that of Spiro-*m*F is shown in the DFT study results).

We also evaluated the charge dynamics occurring at the perovskite-HTM interface using steady-state photoluminescence (PL) and time-resolved PL (TRPL) decay measurements. Figure S19A shows that upon depositing HTM on the perovskite film, the intensity of the steady-state PL spectrum was largely reduced, and the quenching efficacy followed Spiro-*m*F > Spiro-*o*F > Spiro-OMeTAD, which is consistent with the hole mobility trend. Figure S19B shows the TRPL spectra of the devices based on the each HTM as recorded with the peak emission at 800 nm. The TRPL decay data were modeled by a bi-exponential formula [*Y* = *A*$_1$exp(–*t*/τ$_1$) + *A*$_2$exp(–*t*/τ$_2$)] (*45–47*), as listed in table S6, where fast (τ$_1$) and slow (τ$_2$) decay components are related to nonradiative and radiative recombination, respectively. The fitted decay lifetimes (τ$_1$, τ$_2$) are (1438 ns, 2923 ns), (119 ns, 2210 ns), (104 ns, 2299 ns), and (117 ns, 2305 ns) for perovskite without an HTM, with doped HTM Spiro-OMeTAD, Spiro-*m*F, and Spiro-*o*F, respectively. Fast charge extraction and highly efficient charge-transfer processes are key factors for achieving the best PSC performance. Overall, on the basis of

Fig. 1. Optical and electrochemical characteristics and DFT calculation of HTMs. (**A**) Chemical structures of Spiro-OMeTAD and its fluorinated analogs Spiro-*m*F and Spiro-*o*F. (**B**) UV-Vis absorption spectra of Spiro-OMeTAD, Spiro-*m*F, and Spiro-*o*F in dilute chlorobenzene solution (sol) and as thin films. a.u., arbitrary units; Norm., normalized. (**C**) Molecular energy level alignments. (**D**) Electron density distributions of HOMO and LUMO for Spiro-*m*F and Spiro-*o*F.

enhanced mobility and conductivity (the electrical conductivity data in fig. S20), the presented data demonstrate that the best parameters occur in the Spiro-*m*F–based device.
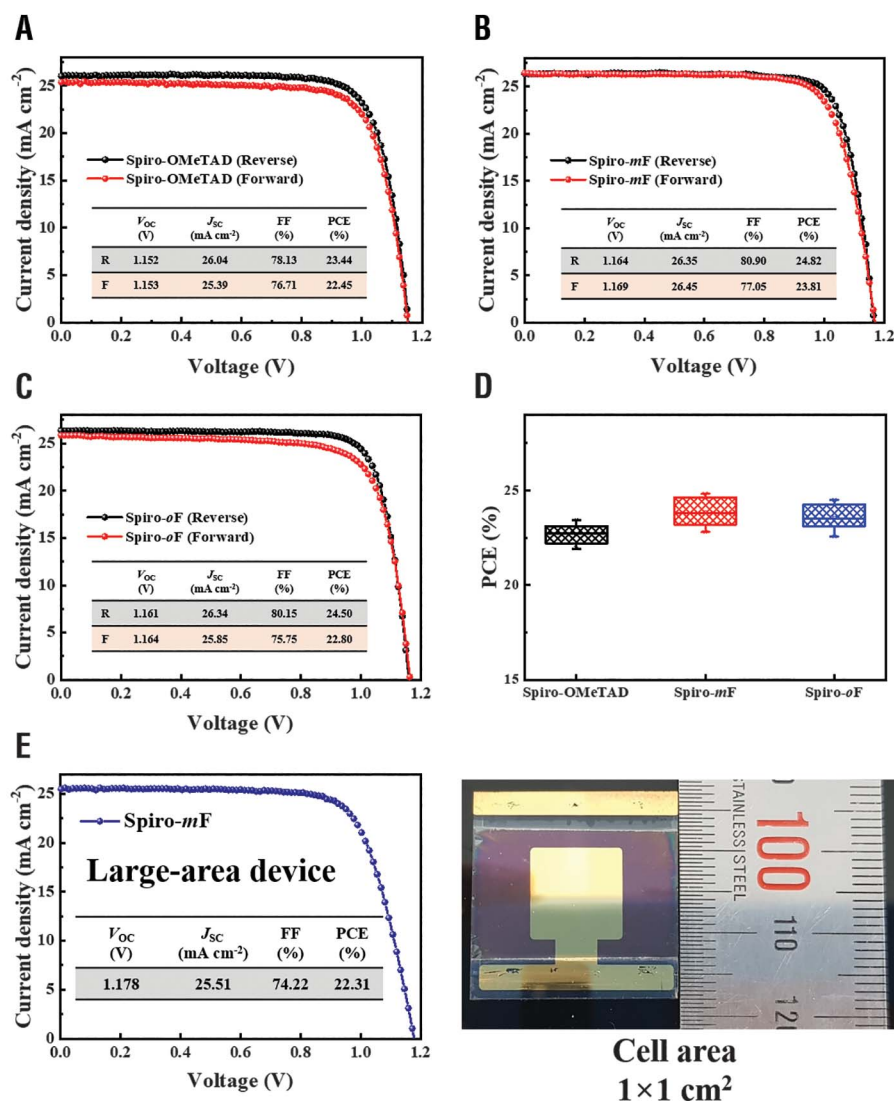
To directly ascertain the degradation processes occurring in perovskite films, we conducted long-term stability tests on the three devices without encapsulation under ~50% RH. The PCE of Spiro-OMeTAD–based control device dropped from 23.21 to 13.74%, corresponding to ~60% of its initial PCE after 500 hours; however, the PCE of both fluorinated HTM-based devices was quite stable, resulting in very high PCE retention (>87%) over the same measurement period. The PCE trends are presented in Fig. 3, and detailed photovoltaic parameters are found in tables S7 to S9. XRD patterns were tracked at regular intervals to estimate the morphological degradation of the device layers (Fig. 3C). The Spiro-OMeTAD–based device exhibited a clear deterioration of the typical perovskite XRD peaks after 500 hours, whereas no apparent impurity peaks were observed in the XRD patterns of devices fabricated with fluorinated HTMs. Moreover, after 3 weeks of storage, no deterioration was observed. From the electrochemical impedance spectroscopy (EIS) analysis with varying times (fig. S21), relative to Spiro-OMeTAD–based device, the fluorinated HTM-based devices, especially for Spiro-*m*F, one discloses smaller EIS resistance values, providing additional proof of their better morphological robustness and charge-transfer behavior. Contact-angle measurements were conducted to determine the surface water resistance of the neat and doped HTM layers on perovskite. As shown in Fig. 3D and table S10, the water droplet contact angle on fluorinated HTM films is larger than that on Spiro-OMeTAD film, indicating reduced hygroscopicity of the fluorine-doped Spiro-*m*F and Spiro-*o*F HTMs. The presence of fluorine atoms induces the creation of kinetic barriers that slow the intrusion of O_2 and H_2O. The increased hydrophobicity generated by using fluorinated Spiro-type HTMs is a key factor contributing to the enhanced stability of PSC devices.

We also conducted in-depth atomistic simulations of the DFT-optimized molecular structures of the three HTMs. When examining the free molecular structures, Spiro-*m*F exhibited a more unfolded structure regarding the angle between the centers of spirobifluorene and two fluorinated methoxyphenyl groups when compared with that of other HTMs (Fig. 4A). We also noticed that the fluorine atoms at the *ortho*-sites caused steric hindrance regarding the free movement of the methoxyphenyl groups. The adsorption state of each HTM on the perovskite surface was investigated by molecular dynamics (MD) simulations (see the "simulation details" section in the materials and methods, as well as Fig. 4B). Spiro-*m*F and Spiro-*o*F adsorbed closer to the perovskite surface than Spiro-OMeTAD, as determined by observing the radial distribution function (RDF) of all phenyl groups on the perovskite surface (fig. S22). In particular, the fluorene

Fig. 2. Photovoltaic performance. *J-V* curves of optimized devices based on (**A**) Spiro-OMeTAD, (**B**) Spiro-*m*F, and (**C**) Spiro-*o*F. (**D**) PCE distribution of each HTM. For each type of device, the solid transverse lines in the boxes are the average values obtained from 15 devices, and the error bars show the highest and lowest values at each point. (**E**) *J-V* curve of the Spiro-*m*F–based device with an area of 1 cm^2 (left); photograph of the device (right).

A

	V_{OC} (V)	J_{SC} (mA cm^{-2})	FF (%)	PCE (%)
R	1.152	26.04	78.13	23.44
F	1.153	25.39	76.71	22.45

B

	V_{OC} (V)	J_{SC} (mA cm^{-2})	FF (%)	PCE (%)
R	1.164	26.35	80.90	24.82
F	1.169	26.45	77.05	23.81

C

	V_{OC} (V)	J_{SC} (mA cm^{-2})	FF (%)	PCE (%)
R	1.161	26.34	80.15	24.50
F	1.164	25.85	75.75	22.80

E

Large-area device

| V_{OC} (V)	J_{SC} (mA cm^{-2})	FF (%)	PCE (%)
1.178	25.51	74.22	22.31

Cell area 1×1 cm^2

units of Spiro-mF were found more on the perovskite surface than that of Spiro-oF (Fig. 4C), implying that the adsorbed structure of Spiro-mF and Spiro-oF could be different. We noticed that Spiro-mF featured a specific RDF peak from the perovskite surface due to the stretched structure of fluorene and phenyl groups on the surface; each peak represents the adsorbed components of Spiro-mF (phenyl and fluorene groups) (fig. S23). On the basis of the configurations sampled from the MD simulations, fluorene and phenyl groups of Spiro-mF adsorbed together on the perovskite surface, whereas those of Spiro-oF often did not adsorb on the perovskite surface together (Fig. 4D). The unfolded structure of Spiro-mF on perovskite is also described by the center-to-end distance (R_{cte}) of the molecule, where the R_{cte} of Spiro-mF and Spiro-oF was ~6.44 and ~5.99 Å, respectively (fig. S24A), indicating that the preservation of the free molecular

Fig. 3. Long-term stability and hydrophobicity.
(**A**) Long-term stability of Spiro-OMeTAD−, Spiro-mF−, and Spiro-oF−based devices in air (~50% RH) without encapsulation. (**B**) Evolution of J-V curves for the unencapsulated PSC devices, based on Spiro-OMeTAD, Spiro-mF, and Spiro-oF over a period of 500 hours. (**C**) Time evolution of XRD patterns of perovskite films with Spiro-OMeTAD, Spiro-mF, and Spiro-oF. (**D**) Contact-angle measurements of pristine and doped HTM films.
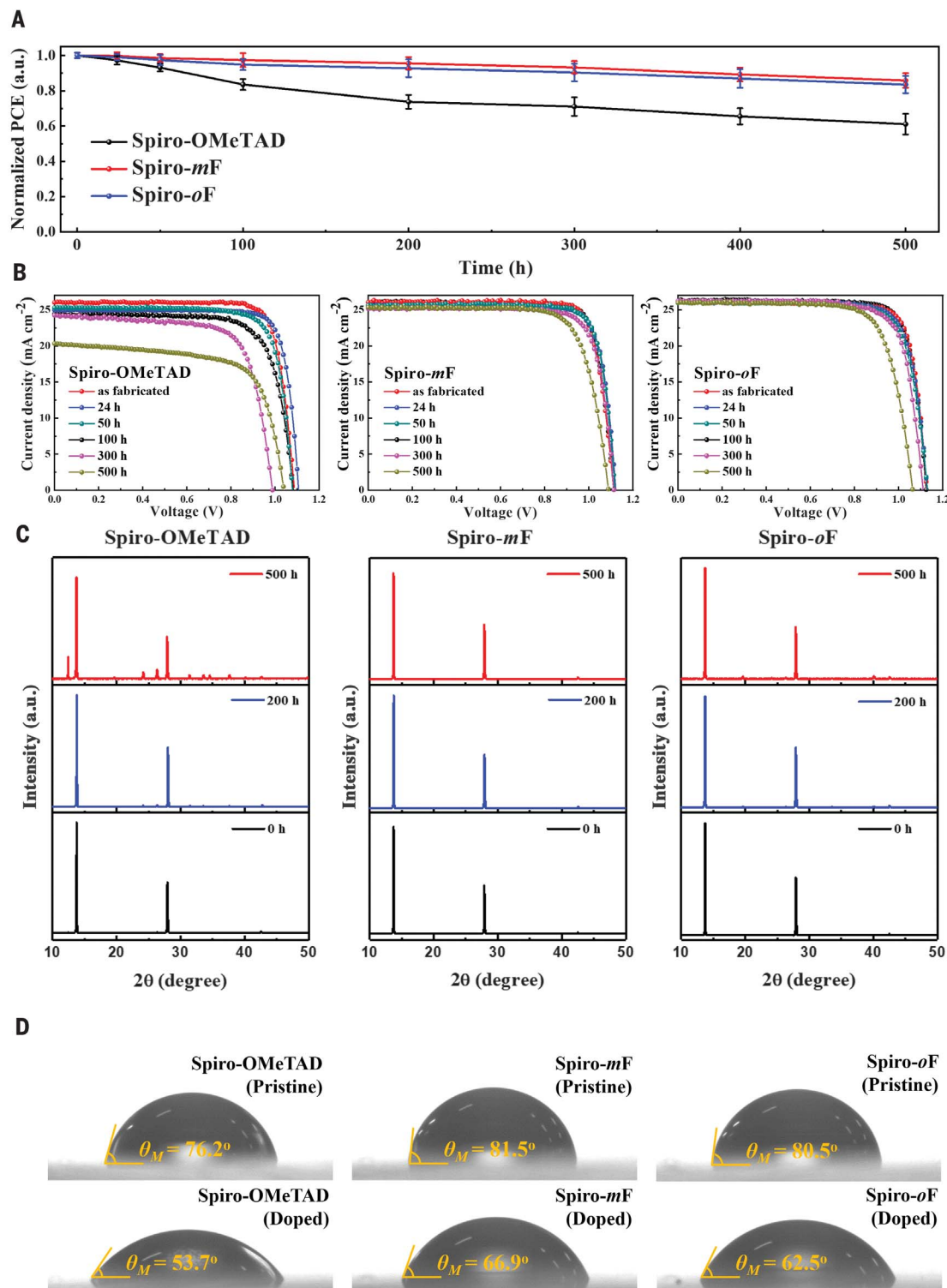
structure of the HTMs occurred on the perovskite surface. The adsorbed Spiro-*m*F molecules were stacked in layers on the perovskite surface, which was revealed by the relative concentration of fluorene groups (fig. S24B). The stacked structure of Spiro-*m*F featured a higher hole-transfer integral (*56* meV) than that of the randomly packed Spiro-*o*F (*29* meV) and Spiro-OMeTAD (*5* meV) on the surface (fig. S24, C and D, and supplementary text 3). The adsorbed Spiro-*m*F, therefore, is considered to be favorable for effective hole
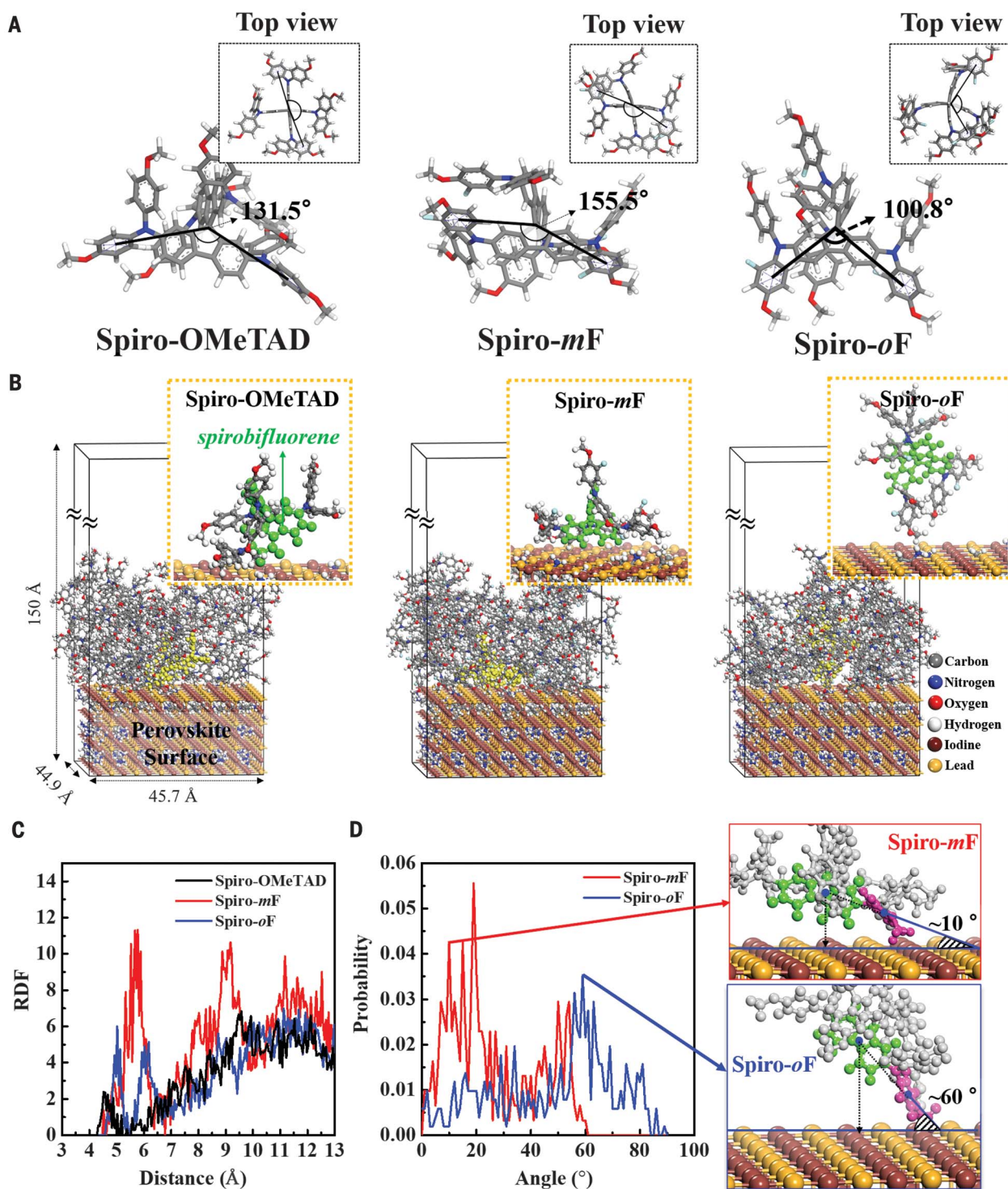
Fig. 4. Molecular simulations. (**A**) Optimized molecular structure of Spiro-OMeTAD, Spiro-*m*F, and Spiro-*o*F. Angles of fluorinated methoxyphenyl groups from the center of spirobifluorene are shown. (**B**) Adsorption structures of Spiro-OMeTAD, Spiro-*m*F, and Spiro-*o*F on the surface of perovskite. Enlarged adsorption states (yellow-colored atoms) are shown in yellow-dotted boxes. (**C**) RDF of fluorene groups and the surface of perovskite. (**D**) Probability distribution of angles of Spiro-*m*F and Spiro-*o*F from the perovskite surface. Red and blue insets show the angles measured with fluorene (green) and phenyl (pink) groups on the surface.

transport (*17*). Along with the detailed atomistic simulations, a comparative investigation of Spiro-OMeTAD versus its fluorinated analogs demonstrates that the fluorination of HTMs with controlled isomerism is a promising strategy to simultaneously achieve high performance and excellent device stability, thus advancing the realization of commercial PSCs.

REFERENCES AND NOTES

1. National Renewable Energy Laboratory, Best research-cell efficiencies chart (2020); www.nrel.gov/pv/assets/pdfs/best-research-cell-efficiencies.20200218.pdf.
2. M. Grätzel, *Acc. Chem. Res.* **50**, 487–491 (2017).
3. N. J. Jeon *et al.*, *Nature* **517**, 476–480 (2015).
4. J.-W. Lee, D.-J. Seol, A.-N. Cho, N.-G. Park, *Adv. Mater.* **26**, 4991–4998 (2014).
5. N. Pellet *et al.*, *Angew. Chem. Int. Ed.* **53**, 3151–3157 (2014).
6. E. A. Alharbi *et al.*, *Nat. Commun.* **10**, 3008 (2019).
7. J. H. Heo *et al.*, *Nat. Photonics* **7**, 486–491 (2013).
8. M. M. Lee, J. Teuscher, T. Miyasaka, T. N. Murakami, H. J. Snaith, *Science* **338**, 643–647 (2012).
9. Y. Liu *et al.*, *Sci. Adv.* **5**, eaaw2543 (2019).
10. J. Burschka *et al.*, *Nature* **499**, 316–319 (2013).
11. N. J. Jeon *et al.*, *Nat. Mater.* **13**, 897–903 (2014).
12. M. Liu, M. B. Johnston, H. J. Snaith, *Nature* **501**, 395–398 (2013).
13. H. J. Snaith, *J. Phys. Chem. Lett.* **4**, 3623–3630 (2013).
14. S. D. Stranks *et al.*, *Science* **342**, 341–344 (2013).
15. N. J. Jeon *et al.*, *J. Am. Chem. Soc.* **136**, 7837–7840 (2014).
16. N. J. Jeon *et al.*, *Nat. Energy* **3**, 682–689 (2018).
17. M. Saliba *et al.*, *Nat. Energy* **1**, 15017 (2016).
18. U. Bach *et al.*, *Nature* **395**, 583–585 (1998).
19. Z. Li *et al.*, *J. Am. Chem. Soc.* **138**, 11833–11839 (2016).
20. J. Liu *et al.*, *Energy Environ. Sci.* **7**, 2963–2967 (2014).
21. F. Zhang *et al.*, *Adv. Energy Mater.* **6**, 1600401 (2016).
22. F. Bella, P. Renzi, C. Cavallo, C. Gerbaldi, *Chemistry* **24**, 12183–12205 (2018).
23. M. Saliba *et al.*, *Energy Environ. Sci.* **9**, 1989–1997 (2016).
24. H. Chen, S. Yang, *J. Mater. Chem. A* **7**, 15476–15490 (2019).
25. L. Fagiolari, F. Bella, *Energy Environ. Sci.* **12**, 3437–3472 (2019).
26. M. Wu, M. Sun, H. Zhou, J.-Y. Ma, T. Ma, *Adv. Funct. Mater.* **30**, 1906451 (2020).
27. Y. Hou *et al.*, *Science* **358**, 1192–1197 (2017).
28. E. H. Jung *et al.*, *Nature* **567**, 511–515 (2019).
29. H. Bin *et al.*, *Nat. Commun.* **7**, 13651 (2016).
30. S. Holliday *et al.*, *Nat. Commun.* **7**, 11585 (2016).
31. Y. Sun *et al.*, *Nat. Mater.* **11**, 44–48 (2012).
32. F. Babudri, G. M. Farinola, F. Naso, R. Ragni, *Chem. Commun.* **2007**, 1003–1022 (2007).
33. I. Benjamin, E. Z. Faraggi, Y. Avny, D. Davidov, R. Neumann, *Chem. Mater.* **8**, 352–355 (1996).
34. H. Bronstein *et al.*, *Chem. Mater.* **25**, 277–285 (2013).
35. G. E. Eperon *et al.*, *Energy Environ. Sci.* **7**, 982–988 (2014).
36. H. Min *et al.*, *Science* **366**, 749–753 (2019).
37. Q. Jiang *et al.*, *Nat. Photonics* **13**, 460–466 (2019).
38. M. Kim *et al.*, *Joule* **3**, 2179–2192 (2019).
39. P. Wang *et al.*, *Adv. Mater.* **32**, e1905766 (2020).
40. S. M. Menke, N. A. Ran, G. C. Bazan, R. H. Friend, *Joule* **2**, 25–35 (2018).
41. W. Shockley, H. J. Queisser, *J. Appl. Phys.* **32**, 510–519 (1961).
42. T. Kirchartz, U. Rau, *Adv. Energy Mater.* **8**, 1703385 (2018).
43. J.-F. Jheng *et al.*, *Adv. Mater.* **25**, 2445–2451 (2013).
44. K. Kawashima *et al.*, *J. Am. Chem. Soc.* **138**, 10265–10275 (2016).
45. Y. Iwata, R. G. Banal, S. Ichikawa, M. Funato, Y. Kawakami, *J. Appl. Phys.* **117**, 075701 (2015).
46. D. Shi *et al.*, *Science* **347**, 519–522 (2015).
47. Y. Yang *et al.*, *Nat. Commun.* **6**, 7961 (2015).

Science

Stable perovskite solar cells with efficiency exceeding 24.8% and 0.3-V voltage loss

Mingyu JeongIn Woo ChoiEun Min GoYongjoon ChoMinjin KimByongkyu LeeSeonghun JeongYimhyun JoHye Won ChoiJiyun LeeJin-Hyuk BaeSang Kyu KwakDong Suk KimChangduk Yang

Operating in wet conditions

The high efficiency of the complex organic molecule Spiro-OMeTAD as a hole-transporting material for perovskite solar cells requires the use of hygroscopic dopants that decrease stability. Jeong *et al.* synthesized hydrophobic fluorinated analogs of Spiro-OMeTAD as hole-transporting materials that have favorable shifting of the electronic state for hole extraction and used them to fabricate perovskite solar cells. A champion device had a certified power conversion efficiency of 24.8% and an open-circuit voltage near the Shockley-Queisser limit. These devices could maintain more than 87% of the original power conversion efficiency under 50% relative humidity for more than 500 hours.

Science, this issue p. 1615

View the article online
https://www.science.org/doi/10.1126/science.abb7167
Permissions
https://www.science.org/help/reprints-and-permissions

Use of this article is subject to the Terms of service